Acta Materialia 292 (2025) 121037

Contents lists available at ScienceDirect

Acta Materialia

journal homepage: www.elsevier.com/locate/actamat

Full length article

# Dynamic fracture response of Cantor-derived medium entropy alloys

Sheron S. Tavares [a], Jesse G. Callanan [b], David R. Jones [b], Daniel T. Martinez [b], James Valdez [b], Aomin Huang [a], Marc A. Meyers [a,*], Saryu J. Fensin [b]

[a] Materials Science and Engineering Program, University of California, San Diego, USA
[b] Center for Integrated Nanotechnologies, Materials Physics Applications Division, Los Alamos National Laboratory, USA

ARTICLE INFO

*Keywords:*
Medium entropy alloys
Spalling
Dynamic fracture

ABSTRACT

The dynamic behavior for five Cantor-derived alloys with four elements in equiatomic composition was investigated. The composition was systematically modified to: CrMnFeNi, MnFeCoNi, CrMnCoNi, CrMnFeCo, and CrFeCoNi. Under identical homogenization, deformation, and recrystallization processing conditions, these materials exhibited significant differences in the microstructure and the corresponding mechanical response, which was measured through uniaxial stress compression loading at strain rates ranging from $10^{-4}$ to $10^{3}$ $s^{-1}$. Additionally, spall recovery experiments were performed at strain rates of ~$10^{4}$ $s^{-1}$ to further understand the effect of strain rate on damage and failure in tension. Four of the five alloys were face-centered cubic and exhibited ductile failure by void nucleation, growth, and coalescence, primarily at the grain boundaries. Surprisingly, the significant differences in compressive strength (ranging from ~200 to ~600 MPa at $10^{-4}$ $s^{-1}$) did not manifest themselves in the spall strength, which varied from 2.08 to 2.61 GPa (not including the CrMnFeCo alloy). This is attributed to similar processes of void growth, which occur at the scale of a few micrometers and do not incorporate the mesoscopic response (such as Hall-Petch), which determines the yield strength. One of the alloys, CrMnFeCo, exhibited especially low ductility in compression and fragmented into pieces during both compression and spall testing. This behavior was attributed to the formation of a brittle Sigma-like phase. The effect of both chemistry and processing was observed to affect the specific spall strength and damage evolution. Specifically, Cr segregation at the grain boundaries had a deleterious effect. This study provides a template for the choice of superior dynamic response among high and medium entropy alloys.

## 1. Introduction

High-entropy alloys, also denoted as multicomponent alloys, ushered a new era in alloy development. The seminal 2004 papers by Cantor [1] and Ye et al. [2] showed that alloys with five equiatomic constituents can have extraordinary mechanical properties, which are generally attributed to five factors:

1. A single-phase solid solution
2. A sluggish diffusion coefficient
3. Severe lattice distortion
4. Short-range ordering around dislocations
5. A low stacking-fault energy, resulting in both dislocations and twins.

In fact, intense research activity led to numerous publications exploring Cantor and other alloys. Prominent are the review articles by George et al. [3], Ye et al. [4], Murty et al. [5], Jien-Wei et al. [6], Tsai and Yeh [7], Zhang et al. [8], and Miracle et al. [9]. Garcia et al. [10] review Medium Entropy Alloys. The total number of publications exceeds 10,000 (web of science). The original ideas were extended to refractory alloys [11–16] and ceramics [17]. The interest in the dynamic response of Cantor alloys is primarily due to potential applications where impact and penetration are involved. Li et al. [18] demonstrated that shear localization is retarded in some of these alloys because of the work hardening exhibited at high strain rates. The topic has recently been reviewed by Huang et al. [19]. Cheng et al. [20] and Wang et al. [21] investigated the dynamic (ballistic and spall) response of a $Fe_{40}Mn_{20}Cr_{20}Ni_{20}$ alloy. Its excellent work hardening capability was cited as a vital factor in its application in ballistic protection.

The dynamic tensile response of a material can be quantified through the measurement of its spall strength, which is the stress required to nucleate voids and/or cracks. in tension. It is an important property of

* Corresponding author.
*E-mail address:* mameyers@ucsd.edu (M.A. Meyers).

https://doi.org/10.1016/j.actamat.2025.121037
Received 31 December 2024; Received in revised form 10 April 2025; Accepted 10 April 2025
Available online 11 April 2025

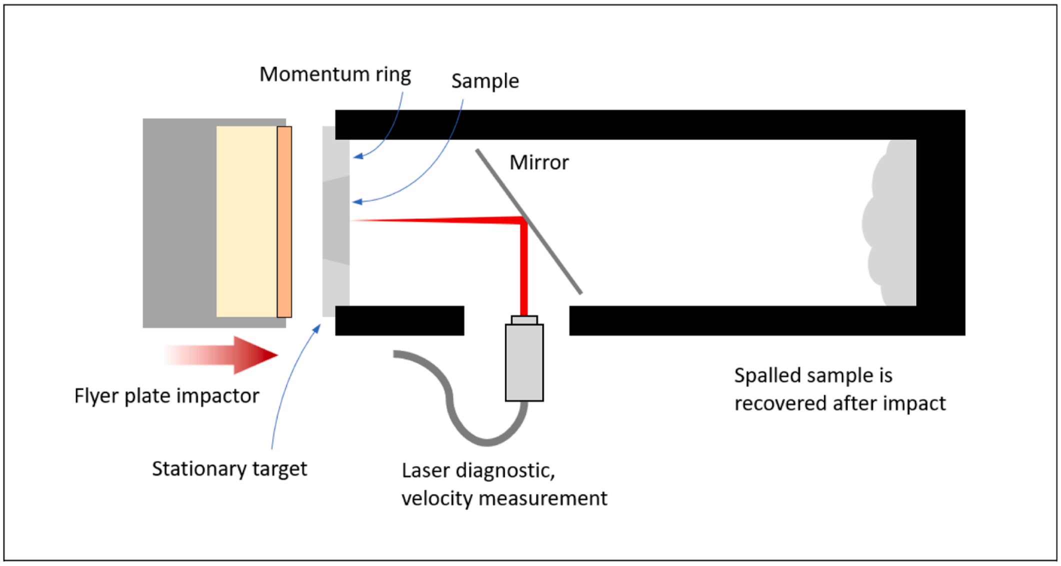


**Fig. 1.** Schematic of gas gun showing flyer plate, target, photon Doppler velocity measurement, and soft recovery tank.

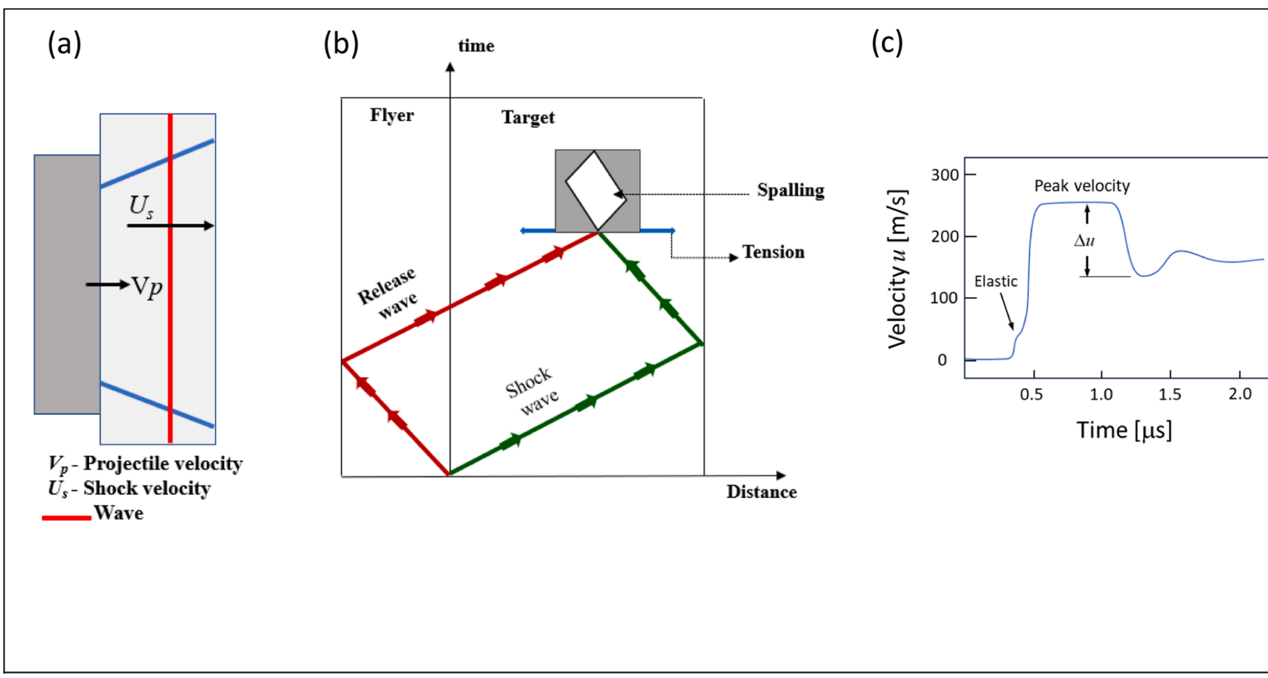


**Fig. 2.** (a) Details of the impact velocity $V_p$ generating a shock wave velocity $U_s$; (b) trajectories of shock wave and release waves in projectile and target and their encounter generating tension and spalling; (c) characteristic free surface velocity captured by PDV gage; the change $\Delta u$ is used to determine spall strength.

metals and can aid in material selection for dynamic environment applications like armor. This dynamic tensile failure, in a uniaxial strain state, does not correlate exactly to the quasistatic failure since other deformation mechanisms become operative at high strain rates [22]. To design materials for these conditions, it is important to understand the role that microstructure plays in damage and failure. There have been numerous studies in metals and alloys to try to understand these relationships [23–26].

However, such studies have been rare in HEAs, and only recently has some work been conducted to establish these relationships in these unique materials. Specifically, there have been recent reports on the spall strength of HEAs [27–29], and the results vary widely depending on the duration of the tensile pulse. Thürmer et al. [30] report on experimental and computational results for the classic equiatomic Cantor alloy. A spall strength of ~8 GPa at the strain rate of $\sim 10^7$ s$^{-1}$ was experimentally measured using pulsed laser shock.

Gas-gun experiments provide a strain rate that is two to three orders of magnitude lower. Five of these experimental results are presented below. A study on the Cantor alloy by Euser et al. [25] measured a much lower spall strength varying between 1.6–2.0 GPa as a function of build parameters in these additively manufactured materials. This was due to the lower strain rate and the presence of initial cracks in the material from the manufacturing process itself. A study by Hawkins et al. [27] on CrMnFeNi further highlighted the importance of manufacturing. This study showed that the spall strength for this alloy was in the 1.3 to 1.9 GPa range, and the failure mechanism under spall was severely brittle due to Cr segregation. Yang et al. [31] report spall strength values of 1.9–2.3 GPa for a $Fe_{50}Mn_{30}Co_{10}Cr_{10}$ alloy. They used a gas gun,

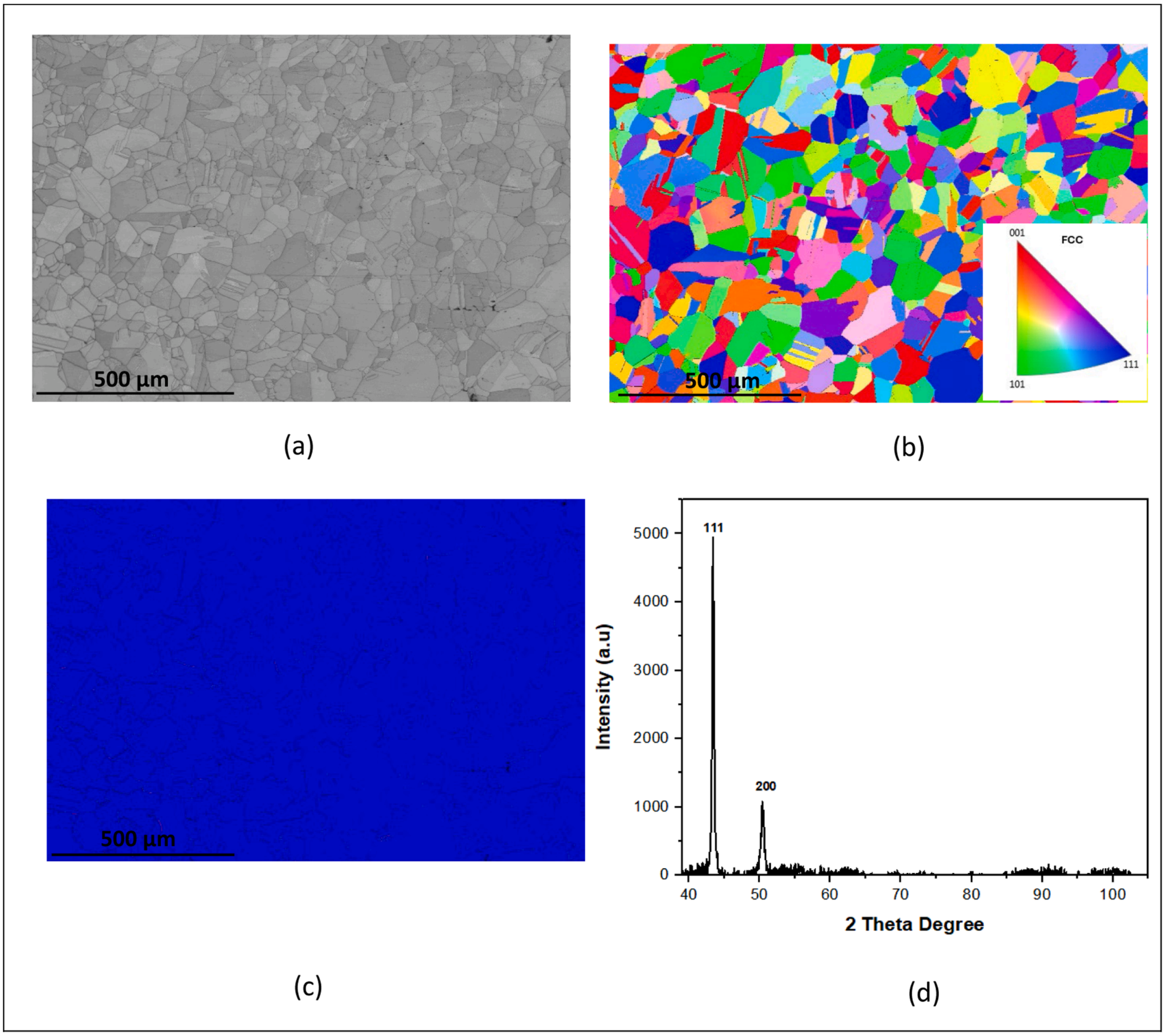


**Fig. 3.** Microstructure of MnFeCoNi after homogenization, deformation, and recrystallization processes. (a) Band contrast; (b) Inverse pole figure of the grain structure; (c) Phase color map; and (d) X-ray diffraction pattern showing a single FCC phase.

providing strain rates varying from $7.5 \times 10^3\ s^{-1}$ to $2.3 \times 10^4\ s^{-1}$. Zhang et al. [29] report higher spall strengths of 3.2–4 GPa for an $Al_{0.1}$CoCrFeNi alloy that has a composition close to one of the alloys used in the current investigation (our CrFeCoNi alloy). The strain rate was higher, ranging from $\sim 1 \times 10^5$ to $\sim 3 \times 10^5\ s^{-1}$. Cui et al. [32] investigated a CrCoNi alloy with large grain size in the mm range and obtained spall strengths that were consistent between different specimens and ranged around 4 GPa, at a strain rate of $\sim 10^5\ s^{-1}$. This strong effect of strain rate will be further discussed in Section 3.

In addition to experiments, molecular dynamics (MD) simulations were used to understand deformation mechanisms in HEAs and how they contribute to damage and failure. These simulations are characterized by a short pulse duration, which results in an extremely high strain rate. MD predicts a spall strength of ~30 GPa at $\sim 10^9\ s^{-1}$ in the Cantor alloy. The value of 30 GPa approaches the cohesive strength, which is the ultimate spall strength calculated from Grady's theory [33]: 35 GPa. The latter value corresponds to the highest strain rate achievable, the Debye frequency. Du et al. [34] obtained values ranging from 11 to 20 GPa at a quoted strain rate of $10^8\ s^{-1}$.

This strength variation for the same alloy can be attributed to the effect of strain rate. Remington et al. [35] and Righi et al. [36] demonstrated that spall strength increases with the strain rate for tantalum and iron, respectively. In fact, the wide variability in the spall strength for a given alloy in the literature can be attributed to the fact that spall strength significantly depends on the specific loading conditions – peak stress, pulse duration, and tensile strain rate, which alter the deformation mechanisms and eventually the stress required to nucleate and grow voids [37]. Due to variation in the loading conditions used to study HEAs, it is difficult to determine the role of a specific chemical composition on the dynamic response.

Thus, the overriding goal of this work is to assess the effect of chemical composition and microstructure on the dynamic response of Cantor-derived alloys using *similar* loading conditions.

In order to accomplish this goal, five medium entropy alloys based on the classic Cantor (CrMnFeCoNi) composition were synthesized and subjected to an identical thermal and mechanical treatment post-manufacturing. This paper presents the quasistatic and dynamic mechanical properties and is organized as follows: Section 2 discusses the experimental methods, Section 3 shows the results, and Section 4 presents our major conclusions.

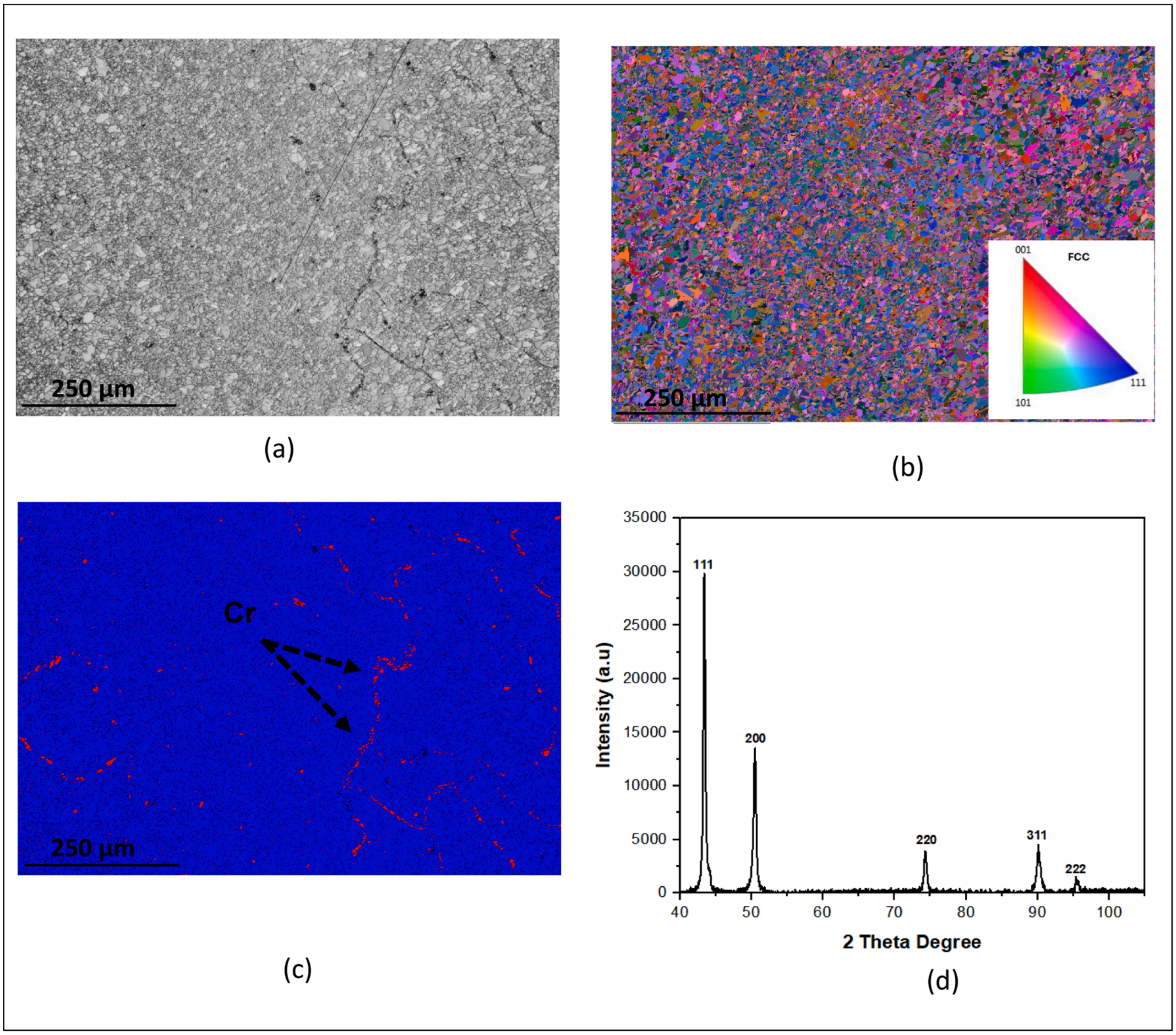


**Fig. 4.** Microstructure of CrMnCoNi after homogenization, deformation, and recrystallization processes. (a) Band contrast; (b) Inverse pole figure of the grain structure; (c) Phase color map showing chromium segregation at grain boundaries (circled); and (d) X-ray diffraction pattern showing a single FCC phase.

## 2. Experimental methods

The five equiatomic four-element alloys were manufactured using induction melting and yielded cylindrical ingots with a diameter of approximately 60 mm. Macroscopic observation showed the presence of dendrites in these as-cast materials. Therefore, the alloys were homogenized at 1150 ºC for 24 h inside stainless-steel bags to minimize oxidation and promote chemical homogenization. The cylinders were subsequently sliced into four sections longitudinally. The smaller segments were deformed to a nominal compressive strain of −0.3 in an Enerpac machine with a 100-ton capacity. The deformation could not be conducted at ambient temperature because the samples cracked; therefore, they were preheated to 400 °C. The samples were subsequently heat treated at 900 ºC for 1 hour in order to ensure recrystallization following deformation. These temperatures were selected due to their successful use in previous studies to ensure the homogenization of chemical elements and recrystallization [38–41]. In the absence of this thermomechanical treatment, the structure with profuse dendrites exhibits poor mechanical properties.

The microstructure was characterized using a field-emission scanning electron microscope (Scanning Electron Microscope (SEM); FEI Apreo Model) equipped with an energy dispersive spectrometer (EDS; Oxford instruments) and electron backscattered diffraction detector (EBSD; Oxford instruments). X-ray diffractometry (XRD; Rigaku Model) was also used to confirm the crystalline structure of the quaternary alloys. The time per step (step size is 0.02º) was 1 s, with a scanning angle from 30º to 100º using Cu-K ($\lambda = 0.154$ nm).

Mechanical testing at low strain rates was conducted on cylindrical specimens prepared by electro-discharge machining with dimensions of 8 mm height and 4.5 mm diameter. These were tested in an Instron uniaxial machine (Model 3367) at strain rates of $10^{-4}$ to $10^{-1}$ $s^{-1}$. For dynamic compression testing, a Split Hopkinson Pressure bar (SHPB) was used with a projectile velocity of approximately 10 m/s. The compression samples had the same diameter as the ones for quasistatic testing (4.5 mm) but a smaller length of 4.5 mm. The strain rate on the Hopkinson bar was approximately $10^{3}$ $s^{-1}$.

High strain-rate tensile loading was performed using a light gas-gun plate impact apparatus [42–44]. An illustration of the system is shown in Fig. 1. The gas gun is a 19.5 mm bore single-stage system equipped with in-situ laser velocimetry and a recovery tank. The samples were machined into shock loading targets of diameter 14 mm with a 5-degree taper and fitted into 304 L stainless steel momentum rings. Since there

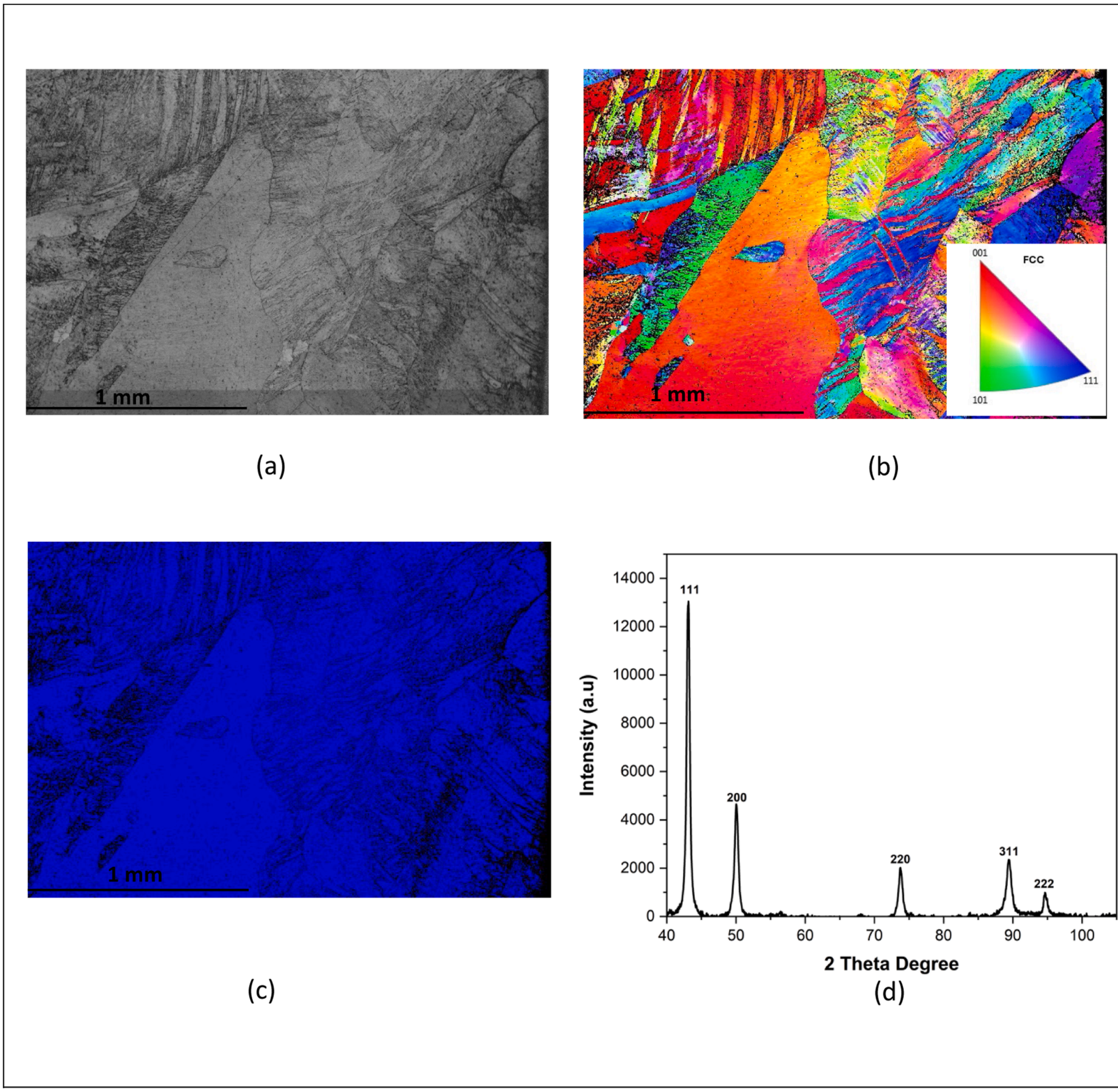


**Fig. 5.** Microstructure of CrMnFeNi after homogenization, deformation, and recrystallization processes. (a) Band contrast; (b) Inverse pole figure of the grain structure; (c) Phase color map; and (d) X-ray diffraction pattern showing a single FCC phase.

was insufficient material available, 304 L was used for momentum rings due to its close impedance mismatch with the target. The targets were machined flat and parallel to a thickness of 3 mm. The finished samples were then held in a stationary target holder and aligned to the barrel axis. The projectiles were fitted with a 304 L stainless steel flyer plate of thickness 1.5 mm and launched down the barrel at speeds on the order of 250 m/s (precise impact velocities are reported for each test later). The sample rear free surface velocity was measured with photon Doppler velocimetry (PDV) [45]. After impact, the sample was ejected from the momentum ring, and the projectile was stopped by the catch tank. The sample was captured and recovered for post-mortem metallographic analysis [46].

An illustration of the concept of the shock loading experiments and an example of the in-situ velocimetry data are shown in Fig. 2. Fig. 2a shows the tapered sample fitted with the momentum ring being impacted by the projectile. The velocity of the projectile and shock wave front are shown. Fig. 2b shows an *x-t* diagram that depicts the wave interactions in a one-dimensional approximation. On impact a shock wave is generated in both the target and the flyer plate. The shock wave propagates into the flyer and, upon reaching the free surface at the rear of the flyer, becomes a release or rarefaction wave. The release wave then propagates back through the flyer and into the sample. A release wave is also generated when the initial shock in the target reaches the target rear free surface. The experiment is designed such that the release wave from the flyer and the release wave from the target surface intersect in the center of the target [47]. When the release waves intersect, the result is the formation of tensile stress that occurs over a very short period of time, i.e., high strain-rate tensile loading, which leads to spall within the target. The shock wave behavior can be investigated via PDV measurement of the rear free surface; an example PDV curve is shown in Fig. 2c. The free surface velocity exhibits an initial elastic wave signal at 0.5 μs followed by a steep rise, which indicates a shock wave breakout at the rear surface. The surface velocity remains at a maximum for a period of roughly 0.5 μs in the example in

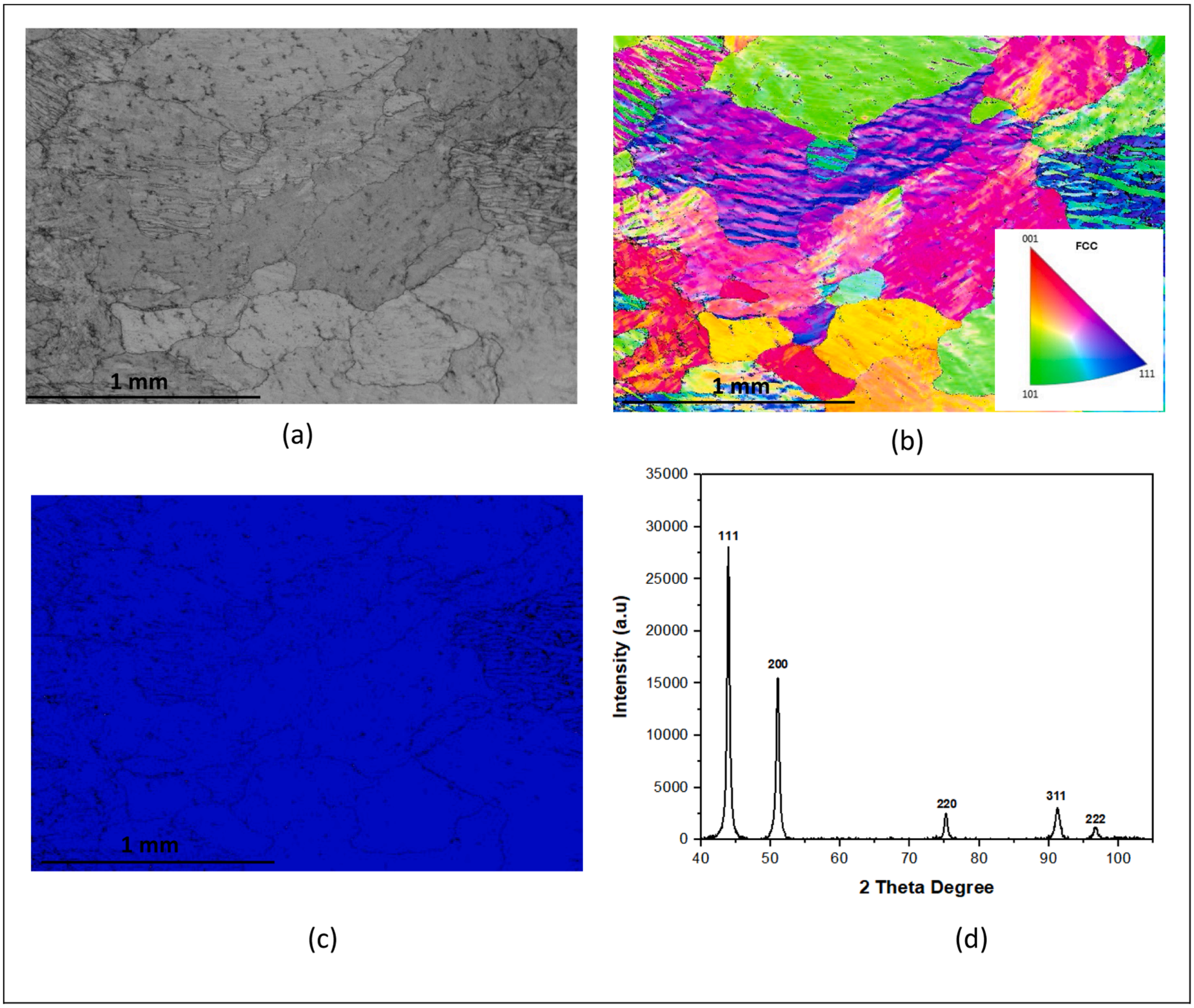


**Fig. 6.** Microstructure of CrFeCoNi after homogenization, deformation, and recrystallization processes. (a) Band contrast; (b) Inverse pole figure shows the orange peel structure within grains and incomplete recrystallization; (c) Phase color map; and (d) X-ray diffraction pattern showing a single FCC phase.

Fig. 2c; from this peak velocity, the peak pressure within the sample can be calculated. The rear sample surface then undergoes a velocity pullback. The magnitude of this velocity pullback is correlated to the spall strength of the material. If the velocity pullback is small, the sample cannot withstand much tensile loading and fails quickly, leading to the free surface maintaining a higher velocity. If the sample has a high spall strength and can withstand high tensile forces at such strain-rates, then the velocity pullback is deep [47], unloading the sample to initial conditions.

## 3. Results and discussion

### 3.1. Microstructural characterization

Although the five alloys were subjected to identical homogenization, deformation, and recrystallization processes, significant microstructural differences were present. These microstructures are shown in Figs. 3–7. Two of the alloys, MnFeCoNi and CrMnCoNi, exhibited fully recrystallized structures with homogeneous and equiaxed grain sizes, measured to be 70 and 6 μm by the linear intercept method (Figs. 3 and 4), respectively. These alloys were single-phase Face Centered Cubic (FCC). However, Cr precipitation at the grain boundaries (Fig. 4c) was observed in CrMnCoNi, which could affect its mechanical response.

CrMnFeNi and CrFeCoNi are essentially single-phase FCC but are only partially recrystallized, as shown by their large grain size on the order of 1 mm and the presence of slip bands (Figs. 5 and 6, respectively). This is close to the compressive specimen diameter (4 mm); the grain size is below the requirement for true polycrystallinity [48], but this cannot be changed. There is significant misorientation, which can be ascertained by the IPFs, which show variations of color inside the grains. These variations are the result of inhomogeneous deformation. Cui et al. [32] determined the spall behavior of medium entropy alloy with similarly large grain size, and this did not result in any inhomogeneity in spall strength, which fluctuated around 4 GPa. The fracture was a mixture of transgranular (when no grain boundary was available) and intergranular (when the position and orientation of the grain boundary coincided with the tensile stress spike). Thus, our confidence in the results is confirmed.

In contrast, the last alloy, CrMnFeCo, had a major presence of a second phase (Fig. 7a and c). This second phase is delineated in Fig. 7a and appears in yellow in the phase color map of Fig. 7c. This second phase is tentatively identified as Sigma, which is known to embrittle alloys. There are also regions (Fig. 7b) that have recrystallized grains. This could be the result of intense localized plastic deformation occurring in the alloy because of large gradients in hardness. The recrystallized grain size of HEAs decreases with plastic deformation (Zheng et al.

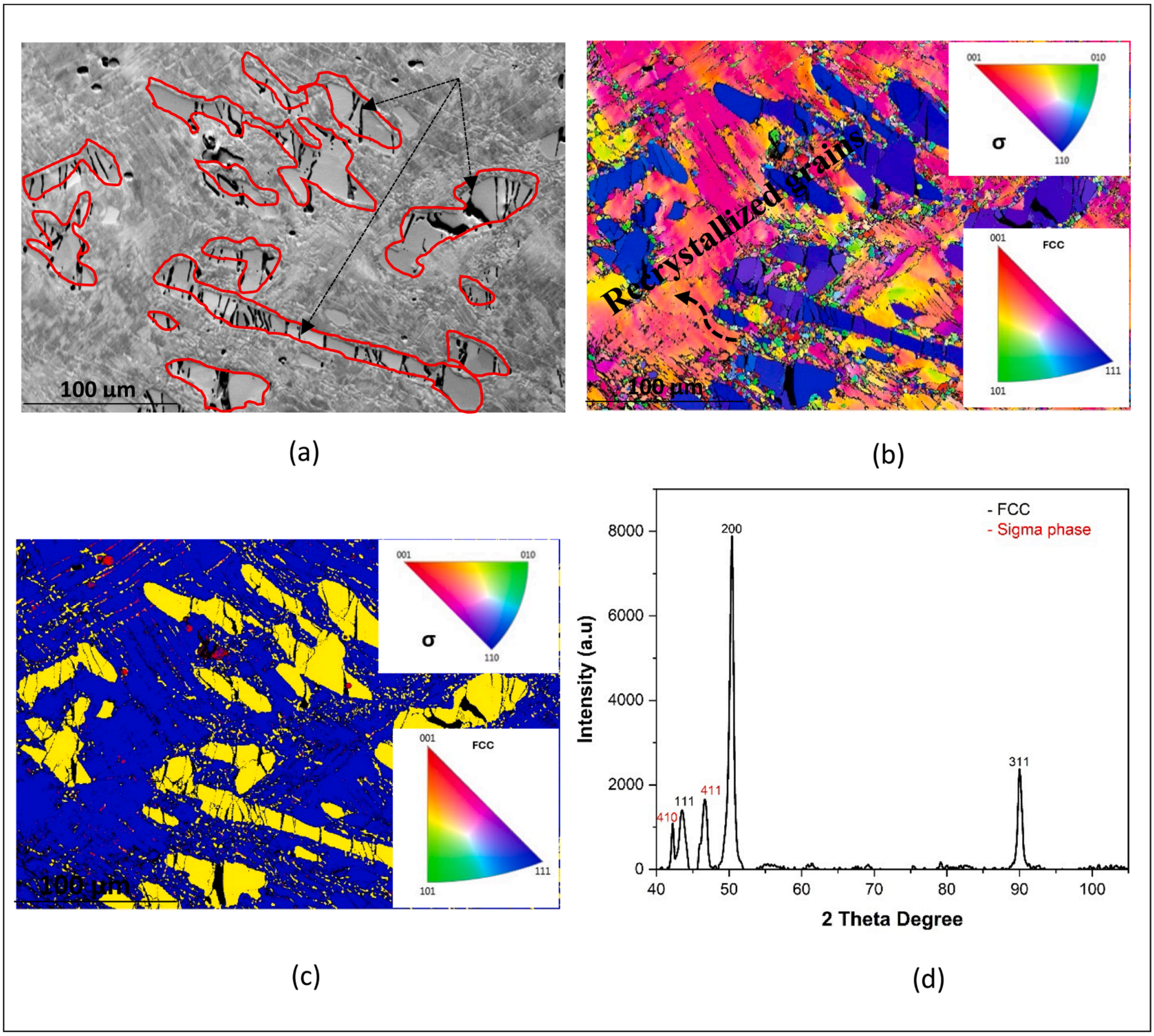


**Fig. 7.** Microstructure of CrMnFeCo after homogenization, deformation, and recrystallization processes. (a) Band contrast; (b) Inverse pole figure of the grain structure showing regions with nanometer-sized grains (indicated in the picture); (c) Phase color map showing a second phase (yellow) with a pattern of microcracks; and (d) X-ray diffraction pattern showing both FCC and a second phase.

[33]), but in certain compositions, the material did not recrystallize and possibly needed either a higher temperature or longer times.

### 3.2. Mechanical response

The hardness across the cross-sections of the five alloys (Fig. 8) shows these differences in the microstructure. MnFeCoNi, which is fully recrystallized with an equiaxed grain structure of random texture (Fig. 3), has the lowest hardness. CrMnCoNi, also fully recrystallized, has a significantly higher hardness due to Hall Petch strengthening. The two partially recrystallized alloys have close hardness (around HVN 250), and finally, the two-phase CrMnFeCo alloy has the highest hardness. There are only minor differences in hardness across the cross-section, except for CrMnFeCo. In this two-phase material, hardness varies from HVN 350 to HVN 375 due to the presence of two phases. The more brittle Sigma phase is harder than the FCC matrix.

The compressive stress-strain curves show the behavior consistent with hardness (Fig. 9a): MnFeCoNi (grain size: 70 μm) has the lowest yield stress of 200 MPa along with the highest work hardening rate. The other fully recrystallized composition with fine grain size, CrMnCoNi, has a yield strength of 470 MPa, which is due to the significant decrease in the grain size (grain size: 6 μm) upon recrystallization. The partially recrystallized composition CrMnFeNi has a yield stress of 450 MPa, due to significant deformation present within the grains. The partially recrystallized CrFeCoNi has a yield stress of 600 MPa, similar to the fine-grained structure, due to significant variation in misorientation within the grains and a residual dislocation structure. Cr segregation in CrMnCoNi probably leads to a decrease in its yield strength compared to its non-segregated counterpart (CrFeCoNi). Finally, the CrMnFeCo two-phase alloy has a yield stress of ~500 MPa and fractures under compression at a strain of 0.3. The work hardening, as quantified by the $d\sigma/d\varepsilon$ vs. $\varepsilon$ curves, shows this behavior in Fig. 9b All conditions show significant initial work hardening, which disappears at a strain of 0.3.

The dynamic stress-strain response, obtained by SHPB measurements (Fig. 10), follows the same trend as the quasistatic experiments: the fully recrystallized MnFeCoNi and CrMnCoNi alloys have yield strengths of 290 MPa and 620 MPa. The partially recrystallized alloy CrMnFeNi and CrFeCoNi have yield stresses of 590 and 670 MPa, respectively. The two-phase alloy CrMnFeCo shows a yield strength (645 MPa) slightly below the CrFeCoNi alloy. The latter alloy did not fracture in the Hopkinson

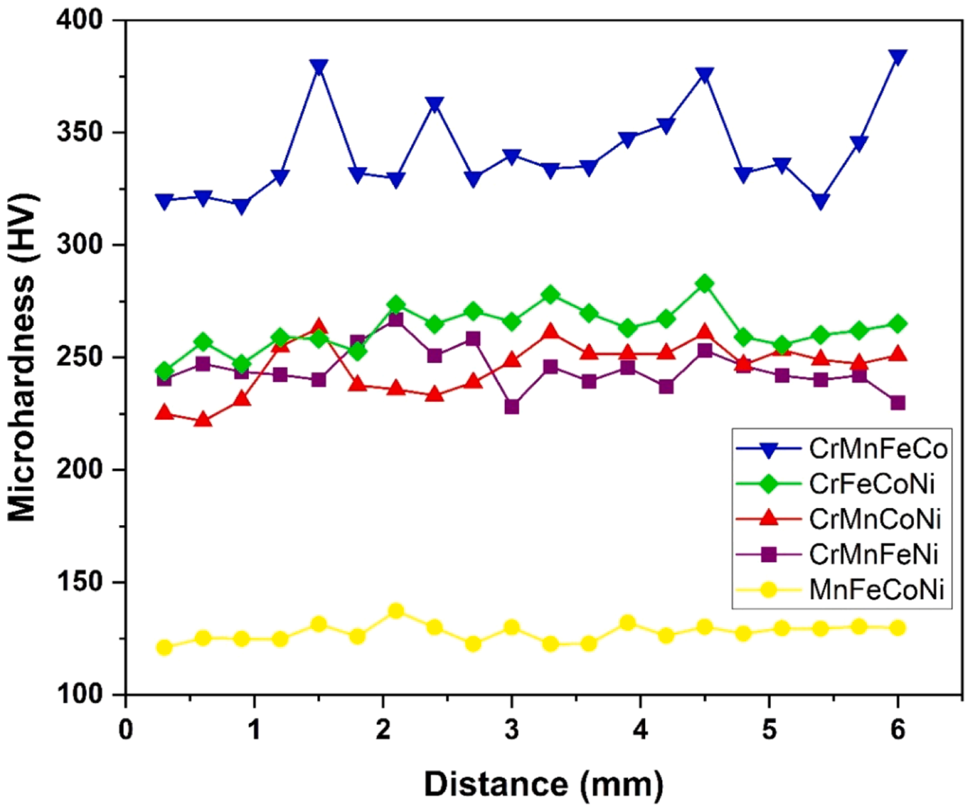


**Fig. 8.** Hardness across cross-section for five alloys. Fully recrystallized MnFeCoNi alloy has the lowest hardness, whereas CrMnFeCo alloy exhibits the highest hardness due to brittle secondary phase. CrFeCoNi, CrMnFeNi, and CrFeCoNi alloys have similar hardness.

bar because the imparted strain is not sufficient ~ 0.1.

A combined plot encompassing the entire strain-rate range of the experiments (Fig. 11) shows an expected increase in flow stress with strain rate. These results are consistent with the strain-rate sensitivity of the Cantor HEA obtained by Park et al. [49]: 0.028. Gangireddy et al. [50] report values of $m = 0.029$ for an $Al_{0.3}CoCrFeNi$ alloy with a grain size of 12 μm and $m = 0.064$ for a grain size of 150 μm. The strain-rate sensitivity $m$ is defined as:

$$m = \frac{log\left(\frac{\sigma_1}{\sigma_2}\right)}{log\left(\frac{\dot{\epsilon}_1}{\dot{\epsilon}_2}\right)} \tag{1}$$

where $\sigma_1$ and $\sigma_2$ are the flow stresses at strain rates $\dot{\epsilon}_1$ and $\dot{\epsilon}_2$, respectively.

The definition used here for $m$ skews the results. As the stress baseline increases, parallel lines exhibit a lower $m$. Therefore, the $m$ values in Fig. 11 decrease with the increasing baseline. There is no atypical response, and the strain-rate sensitivity is the one expected for FCC metals.

These results compare favorably with the Cantor alloy, with values from the literature reproduced in Fig. 11. This is characteristic of FCC metals and alloys in the regime where deformation by dislocation motion is controlled by thermal activation.

The strain-rate sensitivity of the MEAs is consistent with that of stainless steel. Indeed, Hilhorst et al. [51] compare the Cantor HEA with stainless steels 304 L, 316 L, and Invar; they conclude that the latter are superior to the Cantor alloy.

### 3.3. Spall strength

The free surface velocity traces are shown in Fig. 12. The PDV results for most of the samples show an identifiable elastic-plastic transition at the Hugoniot elastic limit, a relatively steep shock rise, and a strong velocity pullback, as expected [44,47]. The exception is CrMnFeCo, which does exhibits a limited velocity pullback and hence shows little to no ductile strength. The dynamic properties under these loading conditions were computed from the free-surface velocity-time data for each sample. The peak stress was calculated using:

$$\sigma_{\text{peak}} = \rho_0 U_s u_p \tag{2}$$

where $U_s$ is the shock wave speed, $u_p$ is the peak particle velocity, and $\rho_0$ is the density at ambient conditions. The shock speed was determined by estimating the impact time using the measured longitudinal elastic wave speed (at ambient conditions), $c_L$, and the time of the elastic wave breakout at the rear free surface (from the PDV results) [27]. The peak particle velocity was estimated as half of the maximum free surface velocity peak value [44]. The ambient density was measured using a precision mass balance and a gas displacement pycnometer (Micrometrics AccuPyc 1330), and the ambient longitudinal, $C_L$, and shear $C_S$, sound speed were measured using an ultrasonic pulse-echo system (Olympus 5072PR). The bulk sound speed can be computed from the longitudinal and shear sound speed as:

$$C_B = \sqrt{{C_L}^2 - \left(\frac{4}{3}\right){C_S}^2} \tag{3}$$

One of the early formulations for the spall strength from the pullback signal is by Romanchenko and Stepanov [52].

Their equation is:

$$\sigma_{sp} = \rho_0 \frac{C_L C_B}{C_L + C_B} \Delta u_{sp} + \frac{\sigma_T}{\tau} x \left(\frac{1}{C_B} - \frac{1}{C_L}\right) \tag{4}$$

Similarly, Eqn. 8 by Zhang et al. [29] is:

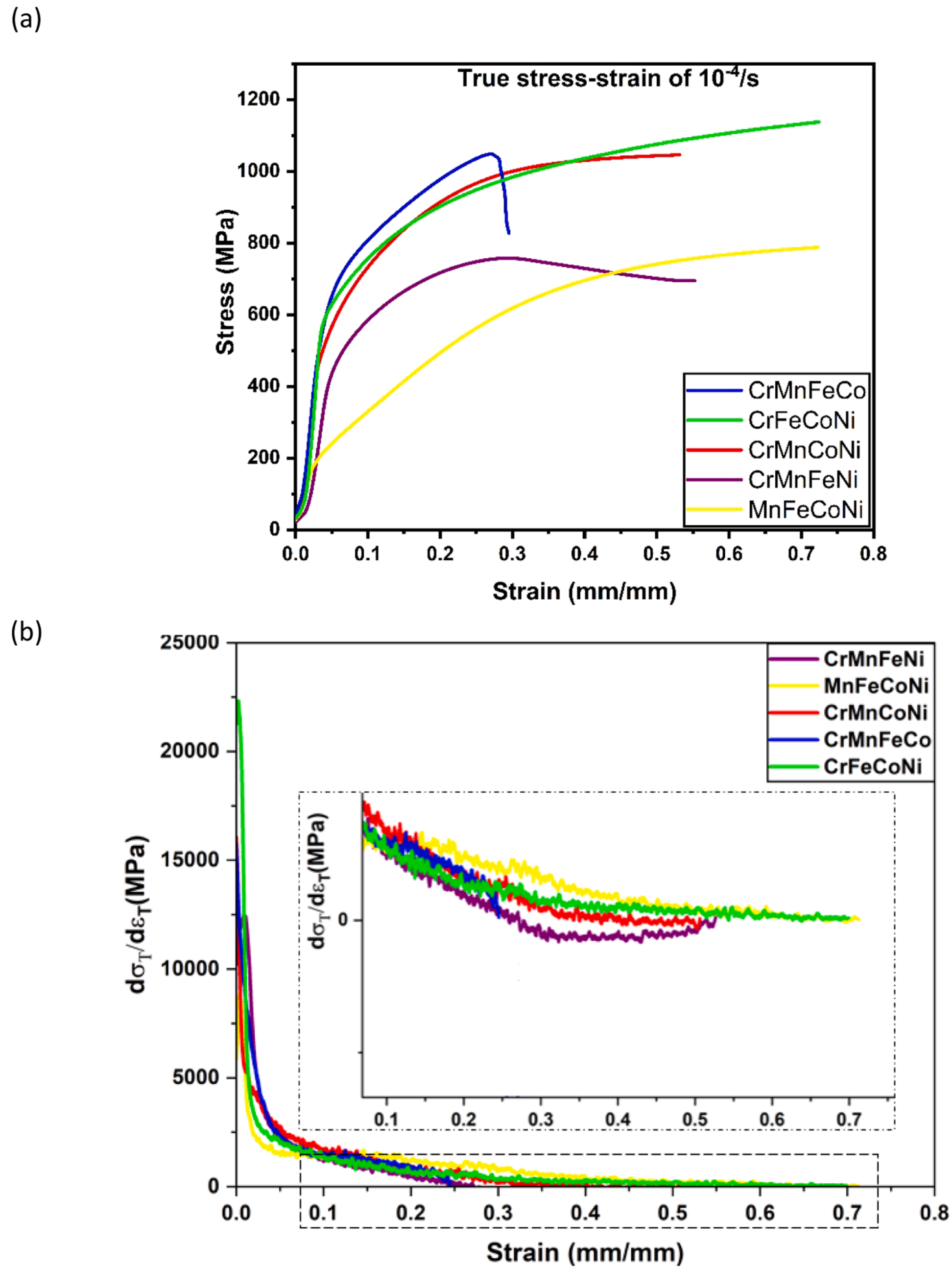


**Fig. 9.** (a) True stress true strain curves for five alloys at $10^{-4}$ $s^{-1}$. Fully recrystallized MnFeCoNi alloy (yellow) has the lowest yield stress. CrMnFeCo alloy, which has a significant fraction of the second, brittle phase, exhibited the highest yield stress but fractured at a strain of 0.3 at $10^{-4}$ $s^{-1}$ (blue curve). Two partially recrystallized single-phase alloys have intermediate strengths. (b) dσ/dε curves as a function of strain for five alloys.

$$\sigma_{sp} \sim \rho_0 C_L \Delta u_{sp} \frac{1}{1+\frac{C_L}{C_B}} \tag{5}$$

where $C_B$ and $C_L$ are the bulk and longitudinal elastic velocities, respectively. $\Delta u_{sp}$ is the pullback signal (the change in free surface velocity from the flat-topped peak stress to the minimum of the pullback region), and $\rho_0$ is the initial density. Cui et al. [32] also use this equation; they reference Antoun et al. [47] as the source. This form is used here, with the bulk sound velocities calculated from Eqn. 3. In our case, the top was not entirely flat, and the maximum of the curve was used. Table 1 shows these values corresponding to the different materials studied here.

The two-phase alloy, CrMnFeCo, completely shattered under shock loading, a tentative spall strength was measured and the sample was not recovered. All the other compositions had similar spall strengths with CoCrMnNi having the lowest spall strength of 2.08 GPa. The lower spall strength of CoCrMnNi can be attributed to the presence of observable Cr-rich particles along the grain boundaries. These particles are initiation sites for grain-boundary decohesion. Even though the spall strength was similar, there were significant differences in the damage morphology between all compositions, as shown in Fig. 13. The spall strengths are given in Table 1.

Specifically, the fully recrystallized alloy (MnFeCoNi) exhibited ductile void nucleation and growth similar to metals like nickel. The spall strength of this material (2.61 GPa) is close to that of polycrystalline nickel (2.9–3.1 GPa [53]). The spall strength of this alloy, at a similar peak stress of ~4 GPa, is somewhat lower than that for alloys like 4340 steel [54] (2.6 to 4.8 GPa), armor steel [55] (4.72 GPa),and HY100

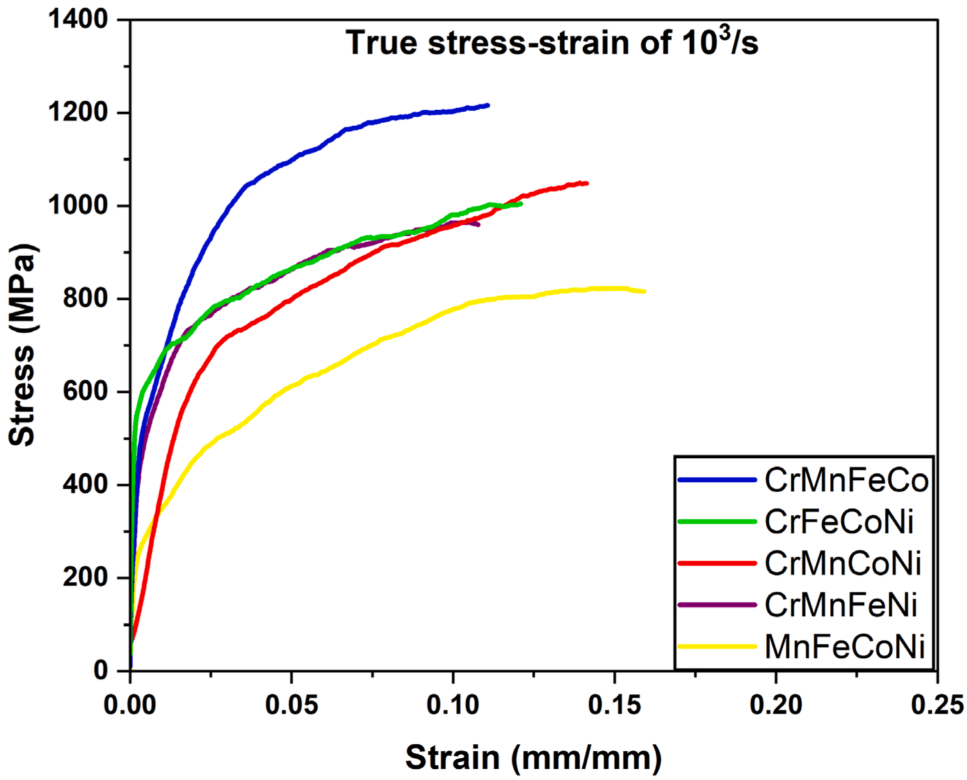


**Fig. 10.** True stress true strain curves for five alloys at $10^3$ $s^{-1}$. Fully recrystallized MnFeCoNi alloy (yellow) has the lowest yield stress. CrMnFeCo alloy, which has a significant fraction of the second, brittle phase, exhibited the highest yield stress and fractured at a strain of 0.13 at $10^3$ $s^{-1}$ (blue curve). Two partially recrystallized single-phase alloys have intermediate strengths.

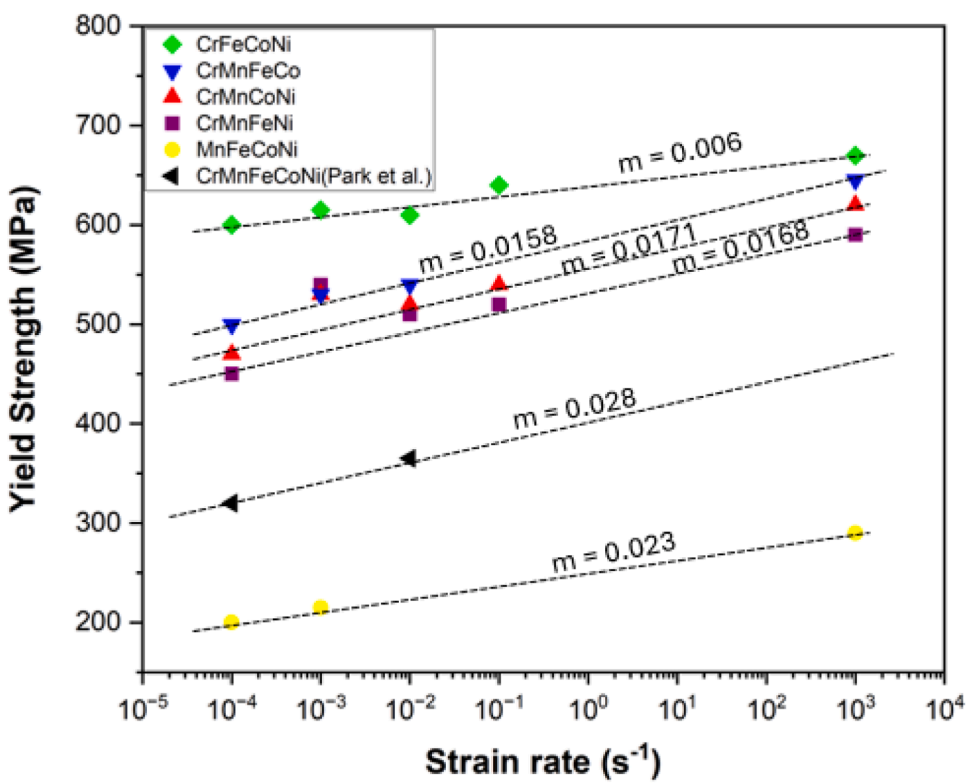


**Fig. 11.** Flow stress of the five alloys as a function of strain rate. The strain rate sensitivity (m) for these alloys varies from 0.006 to 0.023. Park et al. [49] found $m = 0.028$ for CrMnFeCoNi. The strain rate sensitivity was calculated according to the equation below: $m = \frac{\log\left(\frac{\sigma_1}{\sigma_2}\right)}{\log\left(\frac{\dot{\varepsilon}_1}{\dot{\varepsilon}_2}\right)}$.

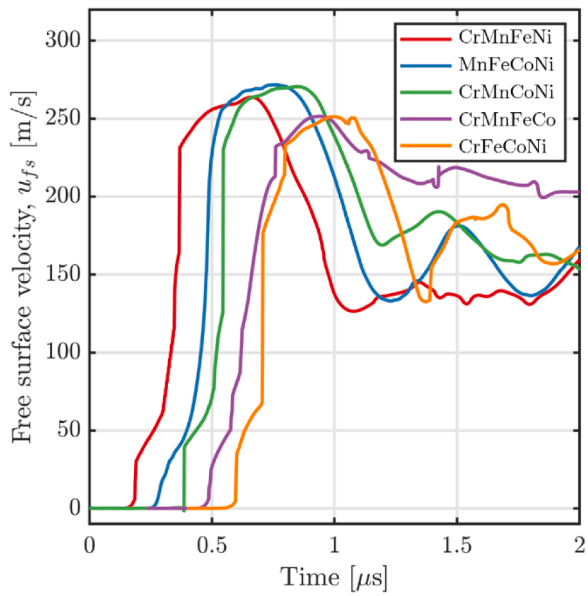


**Fig. 12.** Free surface velocity measurement results for gas gun impact experiments.

[56] (4 GPa). However, differences in the strain rate can change these values significantly; this will be discussed later in this section. Thus, there is no significant increase in spall strength (compared to nickel and steels), suggesting that adding the other elements did not alter the void nucleation and growth mechanisms in this specific alloy, although it did complicate the processing.

However, there might be advantages in terms of the corrosion properties of this MnFeCoNi alloy in comparison to some of the other steels. So, while no overall gains were achieved in terms of dynamic properties by using this specific composition, it also did not cause a decrement in spall strength and can other benefits for the actual applications (these were not pursued as part of this manuscript).

In contrast, the fully recrystallized CrMnCoNi, despite having a finer grain size, exhibited significant Cr segregation, which acted as a source of void nucleation and led to the formation of large “brittle-like” cracks that followed the Cr stringers in the material. Its spall strength was the lowest one of the four recovered conditions: 2.08 GPa. Hence, replacing Fe with Cr was detrimental for the overall dynamic response of this alloy for the particular manufacturing conditions used here. Further heat treatments that re-distribute Cr more homogeneously in the alloy should lead to an increase in the spall strength.

Fig. 14(a) shows the crack opening in CrMnCoNi; the chromium particles (red) are prominent in fracture (EBSD), and the larger particles are more effective in promoting fracture. The fracture surface of (Fig. 14 (b)) follows the Cr particles, the fracture path following chromium particles (see arrows) (SEM). This is unequivocal evidence for failure following the interface between the particles and matrix.

Fig. 15 shows the overall configurations of the separation produced by the tensile pulse. There is a clear tendency for it to occur along grain boundaries, which is the result of two factors: (a) segregation of Cr at the grain boundaries and (b) an inherent increase in the flow stress of the grain interiors due to the strain rate, equaling and exceeding the tensile strength of the grain boundaries.

Of all the five alloys, CrMnFeCo had the most brittle behavior due to the presence of the Sigma phase. Accordingly, the spall strength was much lower than the other four alloys: 0.80 GPa. The two partially recrystallized alloys, CrFeCoNi and CrMnFeNi, had similar spall strengths of 2.56 and 2.57 GPa, respectively. CrFeCoNi displayed a “jagged” brittle failure, as shown by the cracks in the recovered sample, as shown in Fig. 15. This is because the voids nucleated and grew at the grain boundaries between the large grains. We hypothesize that the failure mode was ductile, but the voids grew fast due to the large region in grain boundaries. In CrMnFeNi, the voids were present both at grain boundaries and within the bulk material itself. The additional defects in the grain interior acted as void nucleation sites.

To further understand the reason behind varying damage morphologies observed in these materials, the chemical distribution of elements was evaluated using energy dispersive X-ray spectroscopy (EDS) in the recovered spall samples. This analysis showed that all the HEAs with Cr had a significant segregation of this element within the microstructure. The regions with high Cr concentration also correlated with regions that showed void nucleation and growth. The compositions CrMnCoNi and CrFeCoNi had the most significant amount of Cr segregation, as shown in Fig. 13. It is well investigated that Cr has a propensity to segregate to grain boundaries, and as the volume fraction of grain boundaries increases, so does this segregation of Cr leading to an embrittlement effect. In contrast, CrMnFeNi has a much larger grain size and while Cr segregation is present and does correspond with the void nucleation and growth, it happens at a much smaller scale. This is further reinforced by the fact that the only composition without Cr, MnFeCoNi, showed

**Table 1**
Shock loading experiment results showing sample composition, projectile impact velocity ($v_{imp}$), ambient density ($\rho_0$), longitudinal sound speed ($c_L$), shear sound speed ($c_S$), estimated shock wave speed ($U_s$), Hugoniot elastic limit ($\sigma_{HEL}$), spall strength ($\sigma_{sp}$), and peak stress ($\sigma_{peak}$).

| Composition | $v_{imp}$ (m/s) | $\rho_0$ (g/cc) | $c_L$ (m/s) | $c_S$ (m/s) | $c_B$ (m/s) | $\Delta U_{fs}$ (m/s) | $U_s$ (m/s) | $\sigma_{HEL}$ (GPa) | $\sigma_{sp}$ (GPa) | $\sigma_{peak}$ (GPa) |
|---|---|---|---|---|---|---|---|---|---|---|
| CrMnFeNi | 261 | 7.71 | 5680 | 3070 | 4438 | 134 | 4330 | 0.67 | 2.57 | 4.40 |
| MnFeCoNi | 258 | 8.07 | 5330 | 2960 | 4090 | 140 | 4004 | 0.62 | 2.61 | 4.39 |
| CrMnCoNi | 262 | 7.87 | 5670 | 3100 | 4397 | 107 | 4355 | 0.87 | 2.08 | 4.63 |
| CrMnFeCo | 225 | 7.47 | 5700 | 2920 | 4596 | 42 | 4450 | 0.60 | 0.80 | 4.18 |
| CrFeCoNi | 261 | 8.14 | 5940 | 3430 | 4427 | 124 | 4880 | 1.09 | 2.56 | 4.99 |

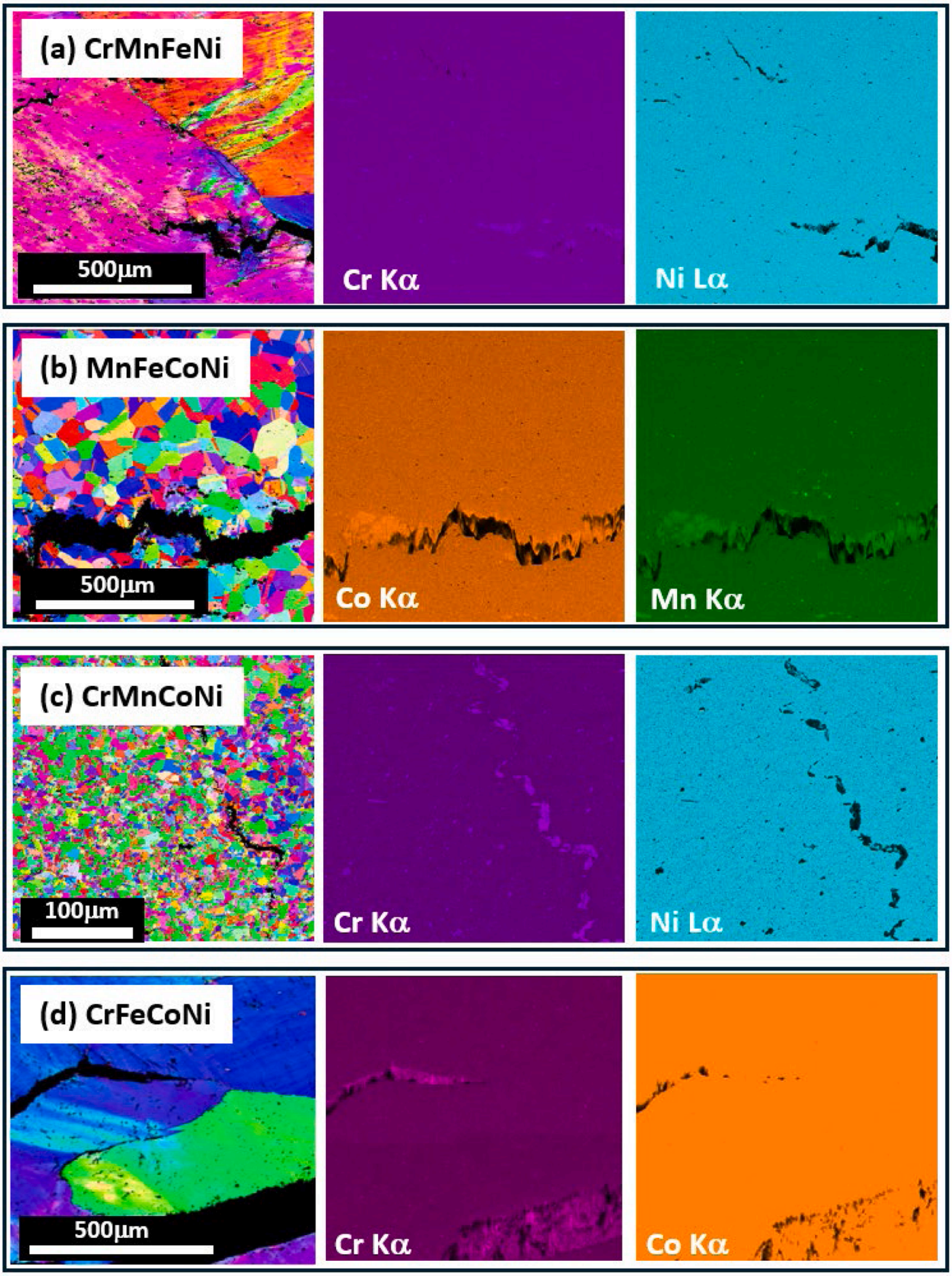


**Fig. 13.** Inverse pole figures and chemistry for recovered MEAs after spall: (a) CrMnFeNi; (b) MnFeCoNi; (c) CrMnCoNi; (d) CrFeCoNi. Only two elements of the EDS maps are shown for clarity, the elements not shown were evenly distributed.

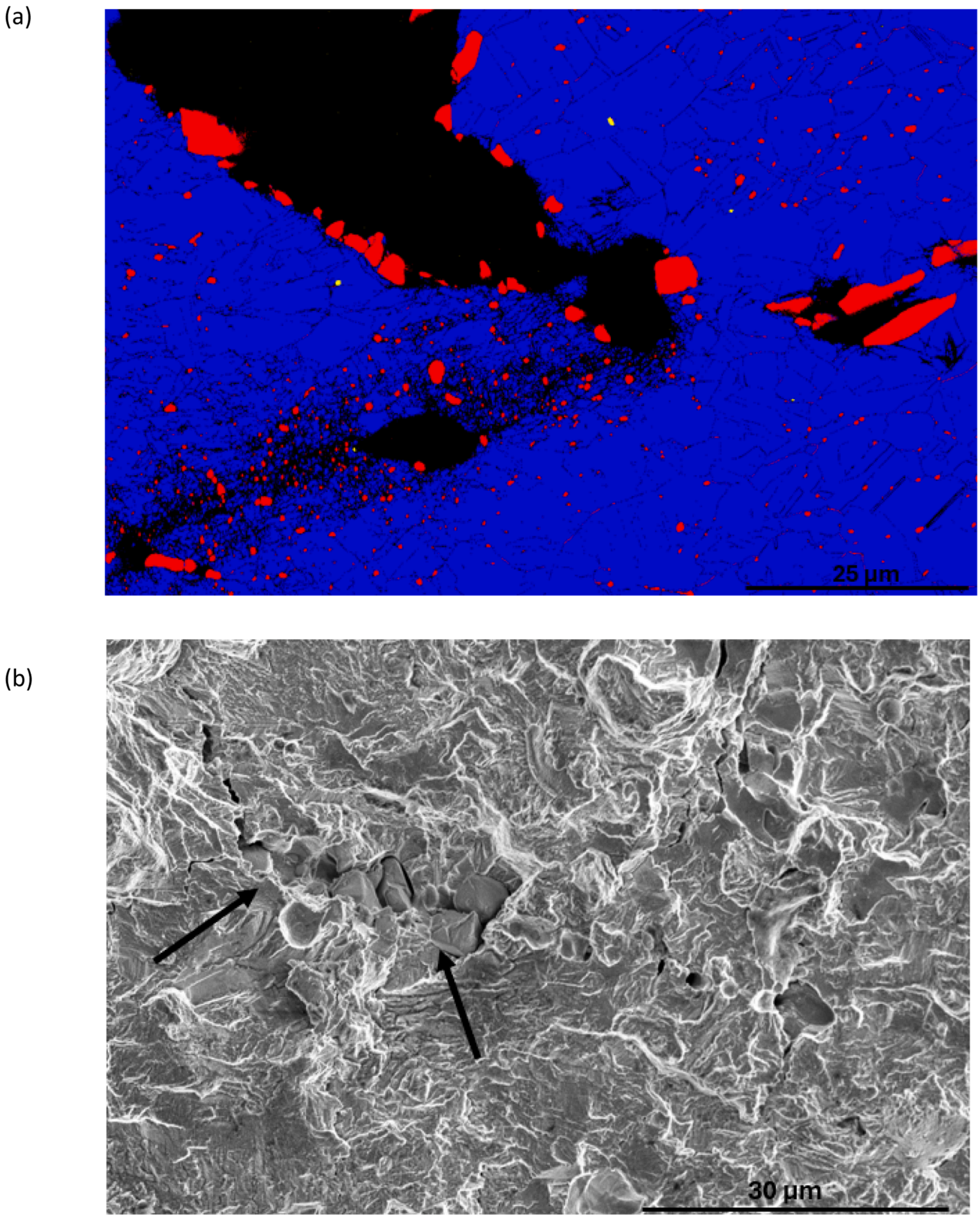


**Fig. 14.** (a) Crack opening in CrMnCoNi; chromium particles (red) are prominent in fracture (EBSD). Larger particles are more effective in promoting fracture. (b) Fracture path following chromium particles (see arrows) (SEM).

classical void nucleation and growth similar to other ductile materials, such as Cu and Ni. The effect of Cr segregation on the compressive behavior of the materials under quasi-static and high strain rate compressive loading is insignificant but affects the spall (tensile) strength significantly. This is because the tensile stresses in spalling produce the interfacial separation between chromium and the matrix.

This work establishes that while composition changes might be a route to modify the dynamic properties of these complex materials, elemental segregation remains an issue and can significantly alter the mechanical and, in particular, the tensile spalling response. Fig. 16 summarizes the current results and compares them with other HEAs at similar and higher strain rates. One previously established fact (Remington et al. [35]; Righi et al. [36]) is that the strain rate plays a very important role in the spall strength. This is the direct consequence of the time dependence of void/crack nucleation, growth, and coalescence. The straight line in the double logarithmic plot tracks the experimental and computational results well. It is interesting to note that the line intersects the ordinate at $10^3$ $s^{-1}$ at a stress of 1 GPa, which is the approximate UTS of the alloys extracted from the Hopkinson bar experiments. The highest value spall strength has been postulated [35,36]

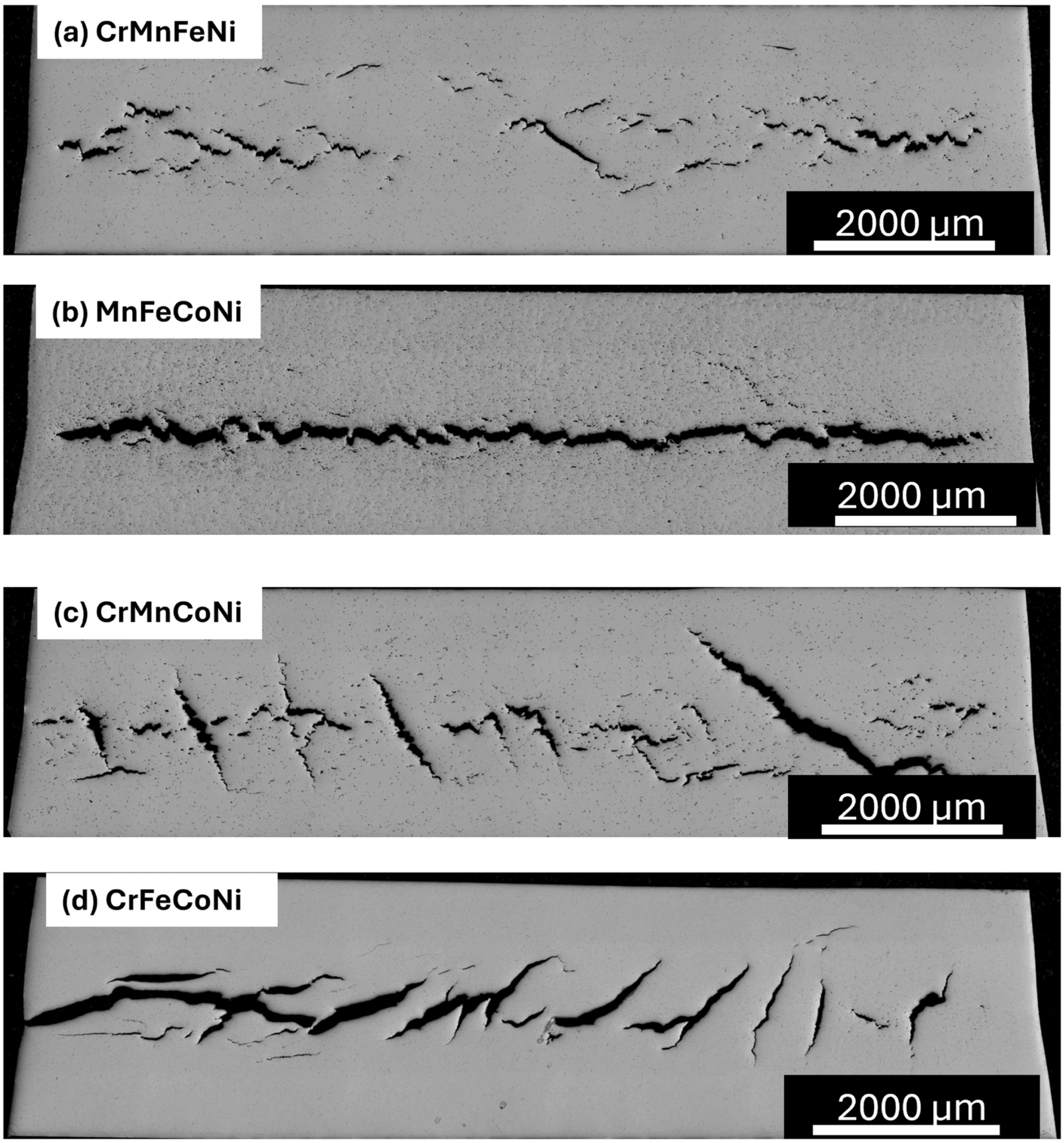


**Fig. 15.** Cross-sections of four alloys after being subjected to spalling experiments. Configurations of cracks in the four alloys follow primarily an intergranular path by virtue of the favored nucleation, growth and coalescence of voids along the grain boundaries.

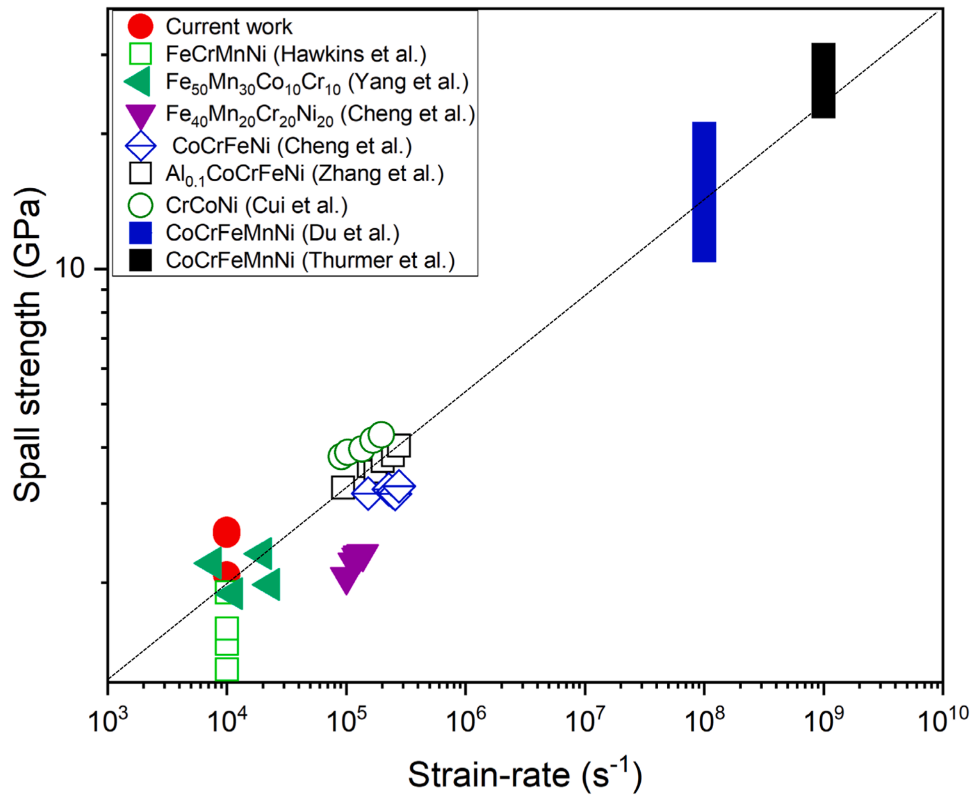


**Fig. 16.** Spall strength as a function of strain rate for HEAs and MEAs; current results are compared with literature values for comparison. The strain rate has a significant effect on spall strength in view of the time dependence of void nucleation, growth, and coalescence.

to be the cohesive strength of the material, and the limit of the strain rate is dictated by the characteristic time for one atom vibration. The latter is given by the Debye frequency. We note that, in addition to the result by Chen et al. [20] for $Fe_{40}Mn_{20}Cr_{20}Ni_{20}$, there is a second report for CoCrFeNi [57]. The results by Hawkins et al. [27] fall under the current spall measurements because their MEA, as discussed earlier, was not homogenized and did not undergo thermomechanical processing. The as-cast microstructure is, therefore, significantly more brittle.

The mechanical response of metals is always complex, and the behavior in spalling is no exception. However, we can delineate some principles that are obeyed by many alloys in spalling experiments, where the strain rate is equal to or higher than $10^4$ $s^{-1}$. Plastic deformation at low strain rates is controlled by the thermally activated motion of dislocations in the alloys studied here. The grain-boundary cohesive strength is higher than the stress required to nucleate and grow voids, and the failure process is transgranular and ductile, yielding dimples. The grain size plays an important effect. At high strain rates, the flow stress is such that failure at grain boundaries is favored. Thus, voids are initiated at these boundaries and propagate along them. This simple schematic explanation is illustrated in Fig. 17. The grain size, which is a dominating effect at low strain rates and is governed by the Hall-Petch equation, is of secondary importance in spalling. Indeed, Jarmakani et al. [58], Remington et al. [35], and Righi et al. [36] obtained higher spall strengths for Va, Ta, and Fe, respectively. In the present experiments, the smaller grain-sized specimen (CrMnCoNi) did not exhibit a higher spall strength than the specimens with large grain sizes. This is connected to the different damage processes occurring in quasistatic and dynamic deformation.

## 4. Conclusions

The Cantor-derived MEAs show, for the same mechanical (compression to a strain of 30 %) and thermal treatment (annealing at 900°C for one hour), a variety of microstructures that generate significant differences in mechanical properties.

- Of the five alloys, only two were fully recrystallized, exhibiting equiaxed grains with two greatly different grain sizes: 6 (for CrMnCoNi) and 70 µm (for MnFeCoNi).
- Like traditional alloys, the microstructure and grain size play a dominant role in the mechanical response of these materials at low strain rates. However, at the high strain rates that occur in spalling, other factors play a role. There is a definite tendency for grain-boundary (intergranular) nucleation and growth being favored over grain-interior (intragranular) processes.
- There is no direct correlation between the compressive strength and the tensile spall strength. Fully recrystallized MnFeCoNi exhibited by far the lowest yield stress, but its spall strength was the highest: 2.61 GPa.
- Chromium segregation was observed in all Cr-containing compositions, which was dependent on grain size. The segregation increased with a decreasing grain size. The CrMnCoNi alloy, which exhibited it to the largest extent, had the lowest spall strength of the four recovered alloys (2.08 GPa).
- The void nucleation sites correlated with regions with high Cr content, principally located at grain boundaries.
- The presence of extraneous phases, such as Sigma, exhibited by the CrMnFeCo is extremely deleterious to the spall strength and should be avoided. The specimens fragmented during compression.
- The spall strengths of the other four compositions vary from 2.08 to 2.61 GPa, excluding the CrMnFeCo, which had a large fraction of the brittle Sigma phase. Both intragranular and intergranular void formation were observed in the failed specimens.

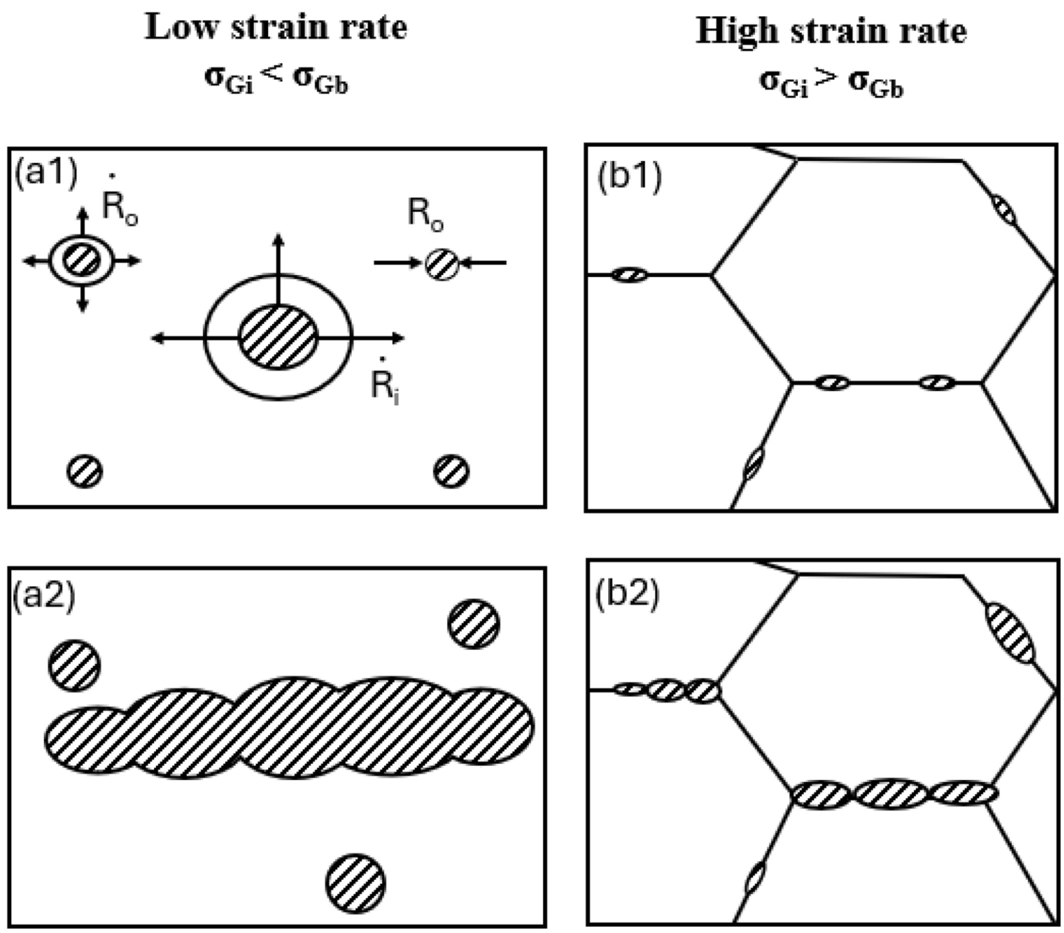


**Fig. 17.** Schematic representation of competing mechanisms of void nucleation and growth: (a) Grain interior initiation; (b) grain-boundary initiation. When the strain rate is low, the stress for grain-interior nucleation is smaller than the stress for grain-boundary nucleation. The reverse occurs at a high strain rate.


## CRediT authorship contribution statement

**Sheron S. Tavares:** Writing – review & editing, Writing – original draft, Methodology, Investigation, Conceptualization. **Jesse G. Callanan:** Writing – review & editing, Software, Methodology, Data curation. **David R. Jones:** Validation, Funding acquisition, Data curation. **Daniel T. Martinez:** Software, Investigation, Data curation. **James Valdez:** Validation, Software, Data curation. **Aomin Huang:** Validation, Software. **Marc A. Meyers:** Writing – review & editing, Writing – original draft, Supervision, Methodology, Investigation, Formal analysis, Data curation, Conceptualization. **Saryu J. Fensin:** Writing – review & editing, Supervision, Investigation, Funding acquisition, Formal analysis, Data curation, Conceptualization.

## Declaration of interests

The authors declare that they have no known competing financial interests or personal relationships that could have appeared to influence the work reported in this paper.

## Acknowledgments

This work was supported by the US Department of Energy through the Los Alamos National Laboratory. Los Alamos National Laboratory is operated by Triad National Security, LLC, for the National Nuclear Security Administration of the U.S. Department of Energy (Contract no 89233218CNA000001). We thank Professor Bingfeng Wang, Central South University, China, for preparing the alloys. We also thank the Center for Matter under Extreme Conditions (CMEC) supported by the Department of Energy National Nuclear Security Administration under Awards DE-NA0004147 and DE-NA0003842.


## References


[1] B. Cantor, I.T.H. Chang, P. Knight, A.J.B. Vincent, Microstructural development in equiatomic multicomponent alloys, Mater. Sci. Eng. A. 375–377 (2004) 213–218, https://doi.org/10.1016/j.msea.2003.10.257.

[2] J.-W. Yeh, S.-K. Chen, S.-J. Lin, J.-Y. Gan, T.-S. Chin, T.-T. Shun, C.-H. Tsau, S.-Y. Chang, Nanostructured high-entropy alloys with multiple principal elements: novel alloy design concepts and outcomes, Adv. Eng. Mater. 6 (2004) 299–303, https://doi.org/10.1002/adem.200300567.

[3] E.P. George, D. Raabe, R.O. Ritchie, High-entropy alloys, Nat. Rev. Mater. 4 (2019) 515–534, https://doi.org/10.1038/s41578-019-0121-4.

[4] Y.F. Ye, Q. Wang, J. Lu, C.T. Liu, Y. Yang, High-entropy alloy: challenges and prospects, Mater. Today. 19 (2016) 349–362, https://doi.org/10.1016/j.mattod.2015.11.026.

[5] B.S. Murty, J.-W. Yeh, S. Ranganathan, P.P. Bhattacharjee, High-entropy Alloys, Elsevier, 2019.

[6] Y.E.H. Jien-Wei, Recent progress in high entropy alloys, Ann. Chim. Sci. Mat. 31 (2006) 633–648.

[7] M.-H. Tsai, J.-W. Yeh, High-entropy alloys: a critical review, Mater. Res. Lett. 2 (2014) 107–123, https://doi.org/10.1080/21663831.2014.912690.

[8] W. Zhang, P.K. Liaw, Y. Zhang, Science and technology in high-entropy alloys, Sci. China Mater. 61 (2018) 2–22.

[9] D.B. Miracle, O.N. Senkov, A critical review of high entropy alloys and related concepts, Acta Mater. 122 (2017) 448–511, https://doi.org/10.1016/j.actamat.2016.08.081.

[10] F.D.C. Garcia Filho, R.O. Ritchie, M.A. Meyers, S.N. Monteiro, Cantor-derived medium-entropy alloys: bridging the gap between traditional metallic and high-entropy alloys, J. Mater. Res. Technol. 17 (2022) 1868–1895, https://doi.org/10.1016/j.jmrt.2022.01.118.

[11] O.N. Senkov, G.B. Wilks, D.B. Miracle, C.P. Chuang, P.K. Liaw, Refractory high-entropy alloys, Intermetallics 18 (2010) 1758–1765, https://doi.org/10.1016/j.intermet.2010.05.014.

[12] O.N. Senkov, G.B. Wilks, J.M. Scott, D.B. Miracle, Mechanical properties of Nb25Mo25Ta25W25 and V20Nb20Mo20Ta20W20 refractory high entropy alloys, Intermetallics 19 (2011) 698–706, https://doi.org/10.1016/j.intermet.2011.01.004.
[13] O.N. Senkov, J.M. Scott, S.V. Senkova, F. Meisenkothen, D.B. Miracle, C. F. Woodward, Microstructure and elevated temperature properties of a refractory TaNbHfZrTi alloy, J. Mater. Sci. 47 (2012) 4062–4074, https://doi.org/10.1007/s10853-012-6260-2.
[14] O.N. Senkov, S.V. Senkova, D.M. Dimiduk, C. Woodward, D.B. Miracle, Oxidation behavior of a refractory NbCrMo0.5Ta0.5TiZr alloy, J. Mater. Sci. 47 (2012) 6522–6534, https://doi.org/10.1007/s10853-012-6582-0.
[15] O.N. Senkov, S.V. Senkova, C. Woodward, D.B. Miracle, Low-density, refractory multi-principal element alloys of the Cr–Nb–Ti–V–Zr system: microstructure and phase analysis, Acta Mater. 61 (2013) 1545–1557, https://doi.org/10.1016/j.actamat.2012.11.032.
[16] J.-P. Couzinié, O.N. Senkov, D.B. Miracle, G. Dirras, Comprehensive data compilation on the mechanical properties of refractory high-entropy alloys, Data Br 21 (2018) 1622–1641, https://doi.org/10.1016/j.dib.2018.10.071.
[17] C. Oses, C. Toher, S. Curtarolo, High-entropy ceramics, Nat. Rev. Mater. 5 (2020) 295–309, https://doi.org/10.1038/s41578-019-0170-8.
[18] Z. Li, S. Zhao, S.M. Alotaibi, Y. Liu, B. Wang, M.A. Meyers, Adiabatic shear localization in the CrMnFeCoNi high-entropy alloy, Acta Mater. 151 (2018) 424–431, https://doi.org/10.1016/j.actamat.2018.03.040.
[19] A. Huang, S.J. Fensin, M.A. Meyers, Strain-rate effects and dynamic behavior of high entropy alloys, J. Mater. Res. Technol. 22 (2023) 307–347, https://doi.org/10.1016/j.jmrt.2022.11.057.
[20] J.C. Cheng, J. Xu, X.J. Zhao, K.W. Shi, J. Li, Q. Zhang, J.W. Qiao, J.Y. Huang, S. N. Luo, Shock compression and spallation of a medium-entropy alloy Fe40Mn20Cr20Ni20, Mater. Sci. Eng. A. 847 (2022) 143311, https://doi.org/10.1016/j.msea.2022.143311.
[21] Z. Wang, X. Jin, H. Yang, J. Qiao, P.K. Liaw, Z. Wang, Mechanical behavior and damage mechanisms of Fe40Mn20Cr20Ni20 high entropy alloys under ballistic impacts, Mater. Sci. Eng. A. 925 (2025) 147874, https://doi.org/10.1016/j.msea.2025.147874.
[22] G.T. Gray III, High-strain-rate deformation: mechanical behavior and deformation substructures induced, Annu. Rev. Mater. Res. 42 (2012) 285–303.
[23] B. MacNider, D. Jones, J. Callanan, M. Beason, G.T. Gray, D.M. Dattelbaum, N. Boechler, S. Fensin, In situ measurement of damage evolution in shocked magnesium as a function of microstructure, Sci. Adv. 9 (2024), https://doi.org/10.1126/sciadv.adi2606 eadi2606.
[24] V.K. Euser, D.R. Jones, D.T. Martinez, J.A. Valdez, C.P. Trujillo, C.M. Cady, S. J. Fensin, The effect of microstructure on the dynamic shock response of 1045 steel, Acta Mater. 250 (2023) 118874, https://doi.org/10.1016/j.actamat.2023.118874.
[25] V.K. Euser, A.S. Mangan, D.R. Jones, D.T. Martinez, T.E. Steckley, A.K. Agrawal, D. J. Thoma, S.J. Fensin, Dynamic spall properties of an additively manufactured, high-entropy alloy (CoCrFeMnNi), Materialia 33 (2024) 101998, https://doi.org/10.1016/j.mtla.2023.101998.
[26] A. Ameri, H. Wang, Z. Li, Z. Quadir, W.D.A. Rickard, M. Gonzalez, P.J. Hazell, J. P. Escobedo-Diaz, Ferrite phase transformation in dual-phase steel under shock loading, Mater. Sci. Eng. A. 802 (2021) 140690, https://doi.org/10.1016/j.msea.2020.140690.
[27] M.C. Hawkins, S. Thomas, R.S. Hixson, J. Gigax, N. Li, C. Liu, J.A. Valdez, S. Fensin, Dynamic properties of FeCrMnNi, a high entropy alloy, Mater. Sci. Eng. A. 840 (2022) 142906, https://doi.org/10.1016/j.msea.2022.142906.
[28] A. Ehler, A. Dhiman, T. Dillard, R. Dingreville, E. Barrick, A. Kustas, V. Tomar, High-strain rate spall strength measurement for CoCrFeMnNi High-entropy alloy, Metals (Basel) 12 (2022), https://doi.org/10.3390/met12091482.
[29] N.B. Zhang, J. Xu, Z.D. Feng, Y.F. Sun, J.Y. Huang, X.J. Zhao, X.H. Yao, S. Chen, L. Lu, S.N. Luo, Shock compression and spallation damage of high-entropy alloy Al0.1CoCrFeNi, J. Mater. Sci. Technol. 128 (2022) 1–9, https://doi.org/10.1016/j.jmst.2022.02.056.
[30] D. Thürmer, S. Zhao, O.R. Deluigi, C. Stan, I.A. Alhafez, H.M. Urbassek, M. A. Meyers, E.M. Bringa, N. Gunkelmann, Exceptionally high spallation strength for a high-entropy alloy demonstrated by experiments and simulations, J. Alloy. Compd. 895 (2022) 162567, https://doi.org/10.1016/j.jallcom.2021.162567.
[31] Y. Yang, S. Yang, H. Wang, Effects of the phase content on dynamic damage evolution in Fe50Mn30Co10Cr10 high entropy alloy, J. Alloy. Compd. 851 (2021) 156883, https://doi.org/10.1016/j.jallcom.2020.156883.
[32] A.R. Cui, S.C. Hu, S. Zhang, J.C. Cheng, Q. Li, J.Y. Huang, S.N. Luo, Spall response of medium-entropy alloy CrCoNi under plate impact, Int. J. Mech. Sci. 252 (2023) 108331, https://doi.org/10.1016/j.ijmecsci.2023.108331.
[33] D.E. Grady, The spall strength of condensed matter, J. Mech. Phys. Solid. 36 (1988) 353–384, https://doi.org/10.1016/0022-5096(88)90015-4.
[34] X. Du, F. Yuan, Q. Xiong, B. Zhang, Q. Kan, X. Zhang, Shock wave response and spall strength in CoCrFeMnNi high-entropy alloy: a molecular dynamics study, Chin. J. Theor. Appl. Mech. 54 (2022) 2152–2160, https://doi.org/10.6052/0459-1879-22-239.
[35] T.P. Remington, E.N. Hahn, S. Zhao, R. Flanagan, J.C.E. Mertens, S. Sabbaghianrad, T.G. Langdon, C.E. Wehrenberg, B.R. Maddox, D.C. Swift, B. A. Remington, N. Chawla, M.A. Meyers, Spall strength dependence on grain size and strain rate in tantalum, Acta Mater. 158 (2018) 313–329, https://doi.org/10.1016/j.actamat.2018.07.048.
[36] G. Righi, C.J. Ruestes, C.V. Stan, S.J. Ali, R.E. Rudd, M. Kawasaki, H.-S. Park, M. A. Meyers, Towards the ultimate strength of iron: spalling through laser shock, Acta Mater. 215 (2021) 117072, https://doi.org/10.1016/j.actamat.2021.117072.
[37] W.D. Turley, S.J. Fensin, R.S. Hixson, D.R. Jones, B.M. La Lone, G.D. Stevens, S. A. Thomas, L.R. Veeser, Spall response of single-crystal copper, J. Appl. Phys. 123 (2018) 55102, https://doi.org/10.1063/1.5012267.
[38] Z. Wu, H. Bei, F. Otto, G.M. Pharr, E.P. George, Recovery, recrystallization, grain growth and phase stability of a family of FCC-structured multi-component equiatomic solid solution alloys, Intermetallics 46 (2014) 131–140, https://doi.org/10.1016/j.intermet.2013.10.024.
[39] Z. Wu, H. Bei, G.M. Pharr, E.P. George, Temperature dependence of the mechanical properties of equiatomic solid solution alloys with face-centered cubic crystal structures, Acta Mater. 81 (2014) 428–441, https://doi.org/10.1016/j.actamat.2014.08.026.
[40] N.D. Stepanov, D.G. Shaysultanov, M.S. Ozerov, S.V. Zherebtsov, G.A. Salishchev, Second phase formation in the CoCrFeNiMn high entropy alloy after recrystallization annealing, Mater. Lett. 185 (2016) 1–4, https://doi.org/10.1016/j.matlet.2016.08.088.
[41] G. Laplanche, P. Gadaud, C. Bärsch, K. Demtröder, C. Reinhart, J. Schreuer, E. P. George, Elastic moduli and thermal expansion coefficients of medium-entropy subsystems of the CrMnFeCoNi high-entropy alloy, J. Alloy. Compd. 746 (2018) 244–255, https://doi.org/10.1016/j.jallcom.2018.02.251.
[42] J.G. Callanan, A.N. Black, S.K. Lawrence, D.R. Jones, D.T. Martinez, R.M. Martinez, S.J. Fensin, Dynamic properties of 316l stainless steel repaired using electron beam additive manufacturing, Acta Mater. 246 (2023) 118636, https://doi.org/10.1016/j.actamat.2022.118636.
[43] J.G. Callanan, D.T. Martinez, S. Ricci, B.K. Derby, K.J. Hollis, S.J. Fensin, D. R. Jones, Spall strength of additively repaired 304L stainless steel, J. Appl. Phys. 134 (2023) 245102, https://doi.org/10.1063/5.0177097.
[44] J.G. Callanan, D.T. Martinez, S. Ricci, N.K. Brewer, B.K. Derby, B.J. Lovato, K. J. Hollis, S.J. Fensin, D.R. Jones, Dynamic and quasi-static strength of additively repaired aluminum, J. Appl. Phys. 136 (2024) 95902, https://doi.org/10.1063/5.0222267.
[45] D.H. Dolan, Accuracy and precision in photonic doppler velocimetry, Rev. Sci. Instrum. 81 (2010) 53905, https://doi.org/10.1063/1.3429257.
[46] G.T. Gray III, Shock wave testing of ductile materials, Mech. Test. Eval. (2000) 530–538.
[47] T. Antoun, L. Seaman, D.R. Curran, G.I. Kanel, S.V. Razorenov, A.V. Utkin, Spall Fracture, Springer Science & Business Media, 2006.
[48] M.A. Meyers, K. Chawla, Mechanical Metallurgy: Principles and Applications, 1984.
[49] J.M. Park, J. Moon, J.W. Bae, M.J. Jang, J. Park, S. Lee, H.S. Kim, Strain rate effects of dynamic compressive deformation on mechanical properties and microstructure of CoCrFeMnNi high-entropy alloy, Mater. Sci. Eng. A. 719 (2018) 155–163, https://doi.org/10.1016/j.msea.2018.02.031.
[50] S. Gangireddy, B. Gwalani, R.S. Mishra, Grain size dependence of strain rate sensitivity in a single phase FCC high entropy alloy Al0.3CoCrFeNi, Mater. Sci. Eng. A. 736 (2018) 344–348, https://doi.org/10.1016/j.msea.2018.09.009.
[51] A. Hilhorst, P.J. Jacques, T. Pardoen, Towards the best strength, ductility, and toughness combination: high entropy alloys are excellent, stainless steels are exceptional, Acta Mater. 260 (2023) 119280.
[52] V… Romanchenko, G. Stepanov, No title, J. Appl. Mech. Technol. 21 (1981) 555.
[53] V.K. Golubev, S.A. Novikov, Y.S. Sobolev, N.A. Yukina, Effect of temperature on the strength and fracture of copper and nickel in spalling, Strength Mater 17 (1985) 76–79, https://doi.org/10.1007/BF01532785.
[54] A.K. Zurek, C.E. Frantz, G.T. Gray, The influence of shock pre-strain and peak pressure on spall behavior of 4340 steel. Shock Wave High-Strain-Rate Phenom. Mater, CRC Press, 1992, pp. 759–768.
[55] H. Wang, S. Higgs, A. Ameri, M. Gonzales, B. McDonald, P.J. Hazell, Z. Li, J. P. Escobedo-Diaz, Spall fracture of two high strength armor steels, AIP Conf. Proc. 2272 (2020) 120031, https://doi.org/10.1063/12.0001024.
[56] G.T. Gray, N.K. Bourne, K.S. Vecchio, J.C.F. Millett, Influence of anisotropy (crystallographic and microstructural) on spallation in Zr, Ta, HY-100 steel, and 1080 eutectoid steel, Int. J. Fract. 163 (2010) 243–258, https://doi.org/10.1007/s10704-009-9440-6.
[57] J.C. Cheng, H.L. Qin, C. Li, F. Zhao, R.C. Pan, Q.Y. Wang, Y.L. Bian, S.N. Luo, Deformation and damage of equiatomic CoCrFeNi high-entropy alloy under plate impact loading, Mater. Sci. Eng. A. 862 (2023) 144432, https://doi.org/10.1016/j.msea.2022.144432.
[58] H. Jarmakani, B. Maddox, C.T. Wei, D. Kalantar, M.A. Meyers, Laser shock-induced spalling and fragmentation in vanadium, Acta Mater. 58 (2010) 4604–4628.